

Chapter 7

Flow past a rough surface

7.1 Introduction

At sufficiently low temperatures, liquid helium has two striking properties. Firstly, it flows without viscosity, and secondly, its vorticity is constrained to thin quantised vortices, characterised by their fixed circulation h/m (the ratio of Planck's constant to the mass of the relevant boson - one atom in ^4He and one Cooper pair in $^3\text{He-B}$) and microscopic core radius ξ (0.1 nm in ^4He and 10 nm in $^3\text{He-B}$). This is in contrast to the eddies observed in everyday viscous fluids, which can have arbitrary shape, size and circulation.

Of ongoing experimental and theoretical study is the nature of turbulence in superfluids [284, 133, 137, 135], a state dominated by an irregular tangle of the quantised vortex lines. Despite the fundamental differences between superfluids and classical fluids, the observation of Kolmogorov energy spectra (made famous in the context of classical isotropic turbulence) in superfluid turbulence [284] are suggestive of a deep connection between them. Superfluid turbulence is at present most commonly formed by moving obstacles, including grids [145, 185], wires [146–148], forks [150, 151], propellers [152, 153], spheres [149] and other objects [154]. Despite progress in visualizing the flow of superfluid helium in the bulk [137, 285], including individual vortex reconnections [107], there is little direct experimental evidence about what happens at boundaries. Here vortices are believed to be generated by two mechanisms. Firstly, they can nucleate at the boundary of the vessel or object. When the relative flow speed is sufficiently low, the flow is laminar (potential) and dissipationless. Near curved boundaries, however, vortex nucleation occurs if the local flow velocity exceeds a critical value. Secondly, the vortices can be procreated from so-called 'remnant vortices' which are present in the system since cooling the helium through the superfluid transition. Note that remnant vortices can be avoided using judicious, slow experimental protocols [286].

The nano-scale vortex core in superfluid helium is comparable in size to the typical

roughness of the boundaries of the vessel or stirring object. Unfortunately, the lack of direct experimental information about vortex nucleation at the boundaries and the subsequent vortex-boundary interactions limit the interpretation of experiments. Theoretical progress is challenging and to date has focussed on smooth and idealised surfaces. In principle, the superfluid boundary conditions are straightforward: the superfluid velocity component which is perpendicular to the boundary must vanish at the boundary, whereas the tangential component (in the absence of viscous stresses) can slip. For the latter reason, we do not expect boundary layers, typical of viscous flows. Implementing these superfluid boundary conditions, Schwarz [287] and Tsubota *et al.* [288] found that one or more vortices sliding along a smooth surface can become deflected or trapped by a small hemispherical bump. Such bumps can also serve as nucleation sites for vortices; the local superfluid velocity is raised at the pole of the bump and more readily breaks the critical velocity for vortex nucleation [240]. Moreover, simulations detailed in Chapter 4 reveal that if the bump is elliptically shaped and elongated perpendicular to the imposed flow, the superfluid velocity at the pole is enhanced, reducing the critical velocity for vortex nucleation and increasing the vortex nucleation rate (for a given super-critical imposed flow). We expect therefore that microscopically-small surface roughness may promote the nucleation of vortices at a surface. For pre-existing vortex lines in the vicinity of the surface, there is also indirect experimental evidence of a ‘vortex mill’ mechanism which continuously feeds vorticity into the flow by stretching the existing vortex lines. This mechanism has been shown to work when the spooling vortex, held by pinning sites at the surface, is aligned in the streamwise direction [289].

7.2 Method

To shed light on the microscopic behaviour of superflow near a rough boundary, we work with the three-dimensional profile of a real surface, shown in Figure 7.1. This corresponds to a one square micron region of the surface of a thin NbTi wire used to generate quantum turbulence at Lancaster University, as profiled via atomic force microscopy (AFM) [163]. The surface is rough, with a height up to around 15 nm, and features sharp grooves and steep ridges, likely to have arisen during the etching phase of the wire preparation. We assume that such features are typical of the wires and similar objects used across other superfluid turbulence experiments.

Traditionally, the Vortex Filament Model (VFM) [290] has been used to model the motion of vortex lines in the presence of smooth spherical [291, 292], hemispherical [287, 288] and cylindrical boundaries [293, 222]. However the model is unsuitable for our purposes for several reasons. Firstly, it assumes that the vortex core is infinitesimal compared to any other length scale, which is not the case if the vortex core size and wall roughness are

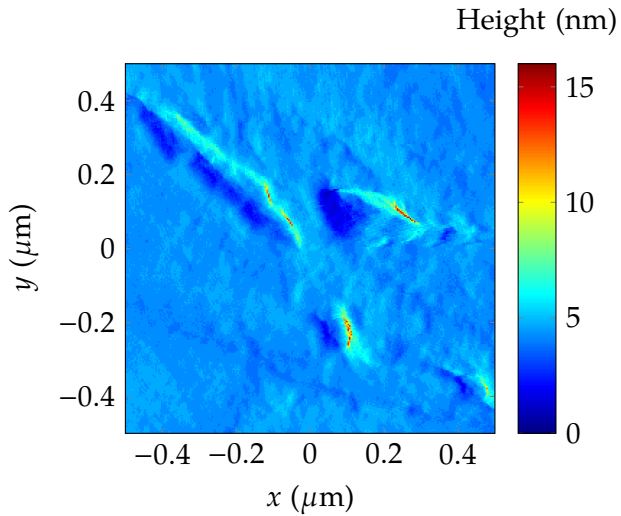


Figure 7.1: AFM image of a section of the NbTi wire used to generate turbulence in superfluid helium at Lancaster University (data provided by R. P. Haley and C. Lawson).

comparable. Secondly, microscopic behaviours such as vortex nucleation or kinetic energy losses due to sound emission are not captured in the model. For example, VFM requires the arbitrary seeding of vortex loops in order to generate turbulence. Thirdly, it is difficult to generalise from smooth, geometrically simple (cylindrical or spherical) boundaries to the rough boundaries which interest us.

Another approach which suffers similar difficulties [294] is the two-fluid Hall–Vinen–Bekarevich–Khalatnikov (HVBK) equations [295, 296]. Moreover, the HVBK equations are coarse-grained over length scales larger than the average vortex separation, hence the boundary conditions require further assumptions or the introduction of unknown sliding/pinning parameters.

We instead model the flow of superfluid helium over this surface through the Gross–Pitaevskii equation (GPE) [165] for a weakly-interacting Bose superfluid, as described in Chapter 2. The GPE is equivalent to a hydrodynamic model with fluid density $n(\mathbf{r}, t) = |\psi(\mathbf{r}, t)|^2$ and local velocity $\mathbf{v}_{\text{loc}}(\mathbf{r}, t) = (\hbar/m)\nabla\theta$, and embodies a classical continuity equation and a modified Euler equation (the modification being the presence of a quantum pressure term, arising from zero-point motion of the particles and is responsible for vortex nucleation). Further details of the hydrodynamic description of the GPE can be found in Section 2.6. While the GPE provides only a qualitative model of the strongly-interacting superfluid helium (for example, the excitation spectrum of the GPE lacks helium’s roton minimum), it nevertheless contains the key microscopic physical ingredients of our problem: a finite-size vortex core, vortex-boundary interactions, and vortex-vortex reconnections [165]. Furthermore, any boundary, however irregular, can be conveniently modelled through the potential term $V(\mathbf{r}, t)$ in the GPE.

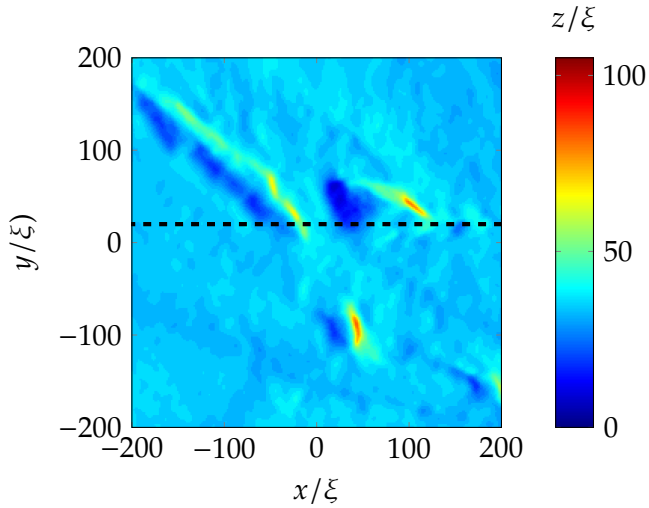


Figure 7.2: AFM image of a section of the NbTi wire rough surface, mapped into the computational coordinate system and smoothed by a Gaussian blur (standard deviation 6 nm) so as to remove discontinuities in the surface profile. The profile used in our 2D simulations ($y = 0.05 \mu\text{m}$) is marked by a dashed line.

The GPE model is numerically simulated in the the homogeneous form as described in Section 2.8.1, and so in this chapter we report quantities scaled by the natural units: the vortex core size is characterised by the healing length $\xi = \hbar/\sqrt{m\rho g}$ and the natural speed, energy and time scales are provided by the speed of sound $c = \sqrt{\rho g/m}$, the chemical potential $\mu = \rho g$ and the unit $\tau = \xi/c$, respectively.

Our results are based on intensive simulations of the GPE over the entire AFM surface, resolved down to a sub-core scale of $\Delta = 0.4\xi$. In ${}^4\text{He}$ the vortex core size is $a_0 \approx 10^{-10} \text{ m}$ [297], such that the AFM image has true core dimensions $(10^4 \times 10^4 \times 100)a_0^3$. It is not computationally feasible to model the corresponding range of scales directly within the GPE; as such we map the AFM image onto the largest practical healing length volume of $(400 \times 400 \times 100)\xi^3$. This is simulated in a box of size $(400 \times 400 \times 200)\xi^3$ (the numerical domain being twice as high as the highest point of the data in the third dimension), on a $1000 \times 1000 \times 500$ spatial grid, which is periodic in x and y . We smooth the original AFM data with a Gaussian blur (standard deviation 6 nm), so as to remove discontinuities in the surface profile, with the result shown in Figure 7.2. The rough surface is then incorporated into the GPE by setting a potential barrier $V = 5\mu$ below the surface, heavily prohibiting density there; above the surface (where $V = 0$) the density recovers to the bulk value ρ over a length scale of the order of ξ . Section 2.15.3 describes the form of V we use in further detail. Additionally, in all our simulations the zero level of the z dimension is arbitrarily shifted so that the minimum height of the two or three-dimensional surface profile is at the level $z = 0$, so as to optimise use of the computational box. The time evolution algorithm is the 4th order Runge-Kutta scheme described in Section 3.1.1 with time step $\Delta t = 0.01\tau$,

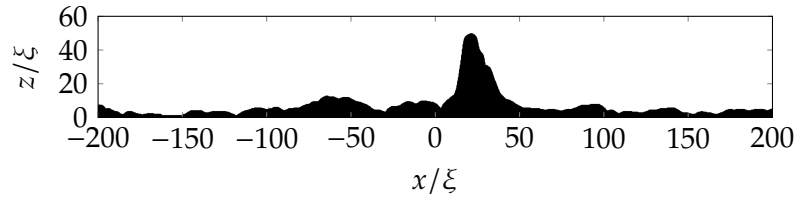


Figure 7.3: The 2D rough surface profile that we employ in our two-dimensional simulations. The surface is taken from the full AFM data so as to capture one of the ‘mountain’ features present on the surface. The data is mapped onto our computational coordinate system as described in Section 7.2 and the exact mapping is shown here.

and is performed across 256 (2.6 GHz) cores of a high-performance computer cluster.

Our three-dimensional simulations model the entire rough surface by using the entire AFM data provided to us, imposed as a potential. However, in the interests of effective exploration of the parameter space, we also perform some simulations in reduced dimensionality. Here we simulate only a single row of the AFM data (marked in Figure 7.2 and shown in detail in Figure 7.3) using the 2D-GPE, ignoring the y dimension. The selected row was chosen so as to contain a two-dimensional analogue of the steep prominences found along the wire’s surface.

We first obtain the stationary solution of the GPE in the presence of the rough boundary, with bulk density ρ . The GPE is then transformed into the frame moving at speed v in the x -direction (equivalent to an imposed flow in the opposite direction) by the addition of a Galilean boost term $i\hbar v \partial\Psi/\partial x$ to the right-hand side of the GPE, as described in Section 2.10.1. The flow speed is ramped up smoothly from zero to the final value of v .

7.3 Two-dimensional results

We begin by focusing on our two-dimensional simulations. For the surface depicted in Figure 7.3, we find the critical velocity for vortex nucleation to be $v_c = (0.125 \pm 0.025) c$. This is significantly less than the critical velocity for a circular obstacle (which has a critical velocity of $v_c \approx 0.38 c$ [140, 223, 225, 226]). This result shows that the effect described throughout Chapter 4 is also occurring for the sharp feature protruding from the rough surface. The location acts as a nucleation site due to the high curvature, which induces a high local fluid velocity, and so Landau’s criterion is broken here before anywhere else in the system. We will refer to such structures that induce this property as ‘mountains’.

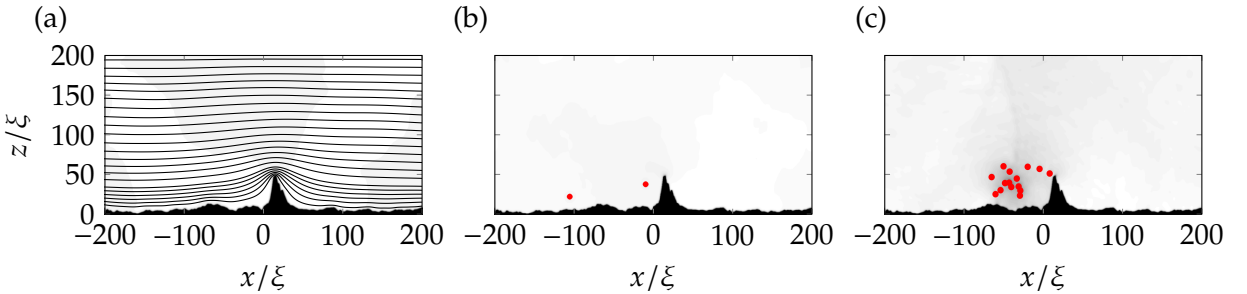


Figure 7.4: Early time evolution of 2D flow past the rough surface for flow speeds (from left to right) of $v = 0.10, 0.15, 0.35 c$. Depicted are snapshots of density and vortex locations at time $t = 500\tau$. Red (blue) symbols represent vortices of positive (negative) circulation. Instantaneous streamlines of the system velocity are also shown in (a).

7.3.1 Vortex nucleation

Early-time vortex nucleation

At early times the resulting flow depends on the velocity of the imposed fluid flow. Below the critical velocity, the fluid undergoes smooth potential flow around the surface. The instantaneous streamlines of this flow, demonstrated in Figure 7.4(a), vary smoothly around the surface with streamlines far away from the surface straight and unaffected by the roughness, and streamlines near the surface showing high curvature.

At velocities above the critical velocity, a series of vortices nucleate from the peak of the highest mountain. The circulation of the vortices produced in the wake of the mountain will depend on the direction of the imposed flow. In our simulations the flow is in the negative x direction and so the produced vortices have positive circulation.

The strength of the imposed flow affects the vortex nucleation frequency, so that for larger flow velocities more vortices are produced in a given time period. This is confirmed by measurement of N_v at different flow velocities, shown in Table 7.1 for this and modified surfaces. For velocities just higher than the critical velocity, vortices nucleate from the mountain at low enough frequency that they fall downstream and do not interact significantly. For high velocities, however, many vortices nucleate in close proximity and interact strongly with one another. Vortex co-rotation is induced and this leads to the vortices combining into a larger-scale cluster of positive circulation. Figure 7.4 shows the early vortex configuration for different imposed flow speeds.

Secondary clusters

For the case where vortices combine into a larger-scale cluster, an interesting effect occurs. Close to the surface, the combined velocity field of the cluster induces a relatively large local velocity in the opposite direction to the imposed flow. This induces a secondary

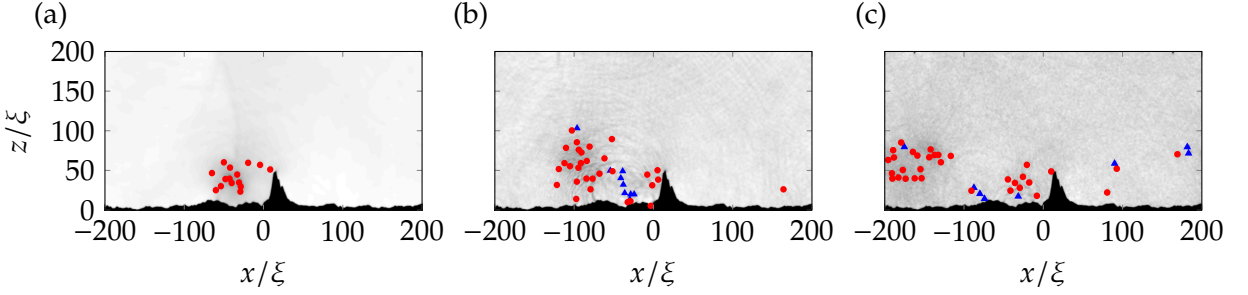


Figure 7.5: Evolution of 2D flow past the rough surface for a flow speed of $v = 0.35c$. Depicted are snapshots of density and vortex locations at times (from left to right) $t = 500, 1580$, and 2100τ . Red (blue) symbols represent vortices of positive (negative) circulation.

generation of vortices from smaller-scale surface prominences. The secondary vortices are of opposite circulation to the cluster that induced them (in our case, negative circulation) and also form a new vortex cluster. As this cluster grows, the velocity field that caused the effect is cancelled out, leading to a cessation of secondary vortex production. Figure 7.5 demonstrates the production of a secondary cluster of negative circulation vortices in a simulation with $v = 0.35 c$. It is important to note that the generation of secondary clusters requires the surface to be rough downstream of the mountain; if the surface is perfectly smooth downstream, there are no secondary nucleation points available to generate new vortices. We also note that it is possible to generate tertiary vortices/clusters; these arise when the secondary cluster induces a sufficiently high flow speed to generate even further vortices from the local surface roughness. Secondary and tertiary vortex nucleation is shown in detail in Figure 7.6, with a schematic overlay describing the process.

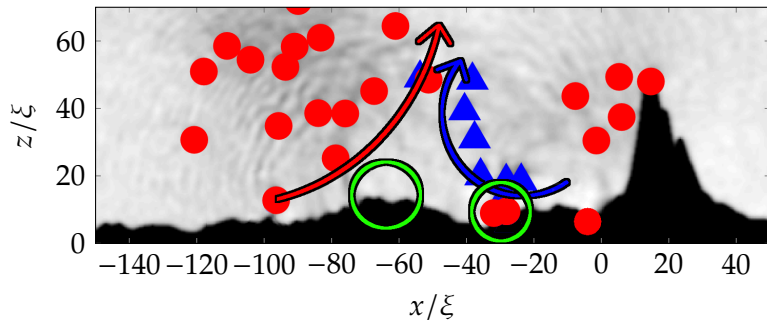


Figure 7.6: Snapshot of fluid density and vortex locations at time $t = 1580 \tau$ with $v = 0.35 c$, demonstrating secondary and tertiary vortex nucleation. Red (blue) symbols represent vortices of positive (negative) circulation. The direction of the vortex cluster velocity field is labelled with red and blue arrows, with the secondary and tertiary nucleation sites circled in green.

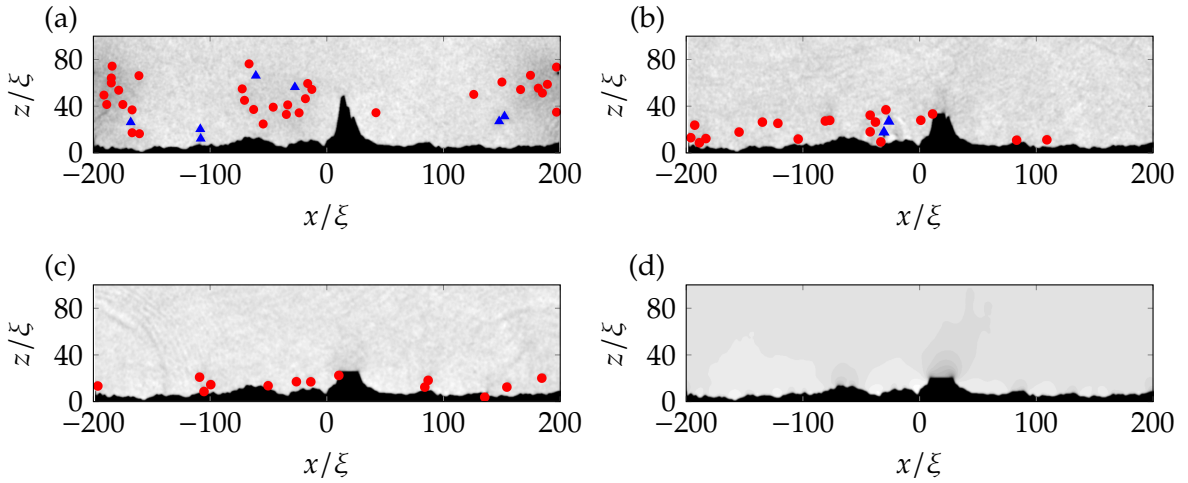


Figure 7.7: Same-time density snapshots for flow speed is $v = 0.35 c$, time $t = 2440\tau$ and various levels of surface truncation: (a) $\beta = 100\%$, (b) $\beta = 70\%$, (c) $\beta = 50\%$ and (d) $\beta = 40\%$, where β represents the truncation height relative to the highest point in the surface. Vortices with positive (negative) circulation are labelled with red (blue) markers.

Truncated surfaces

It is evident by the snapshots shown in Figure 7.4 that the vortex generation is dominated by the large single mountain in the surface. In fact, it can be reasoned that even if the imposed flow v has a high enough velocity that the smaller provinces also act as vortex nucleation sites, the largest mountains will always lead to the largest local velocity and highest vortex nucleation frequency, and so will always be the main producer of vorticity.

To further analyse how the height of the mountains affects fluid flow in the vicinity of a surface, we now describe how the situation changes with truncation of the mountain height, to a percentage β of the maximum height h_0 , i.e. $h(x, y) \rightarrow h(x, y)H(z/h_0 = \beta)$, where $H(z)$ is the Heaviside step function ($\beta = 100\%$ corresponds to no truncation, $\beta = 0$ corresponds to complete truncation). For the AFM image we use, this truncation can be thought of as a way of varying surface roughness by removing the sharpest features.

Figure 7.7 shows snapshots (at fixed time) for various levels of truncation β , with all cases having the same flow speed $v = 0.35 c$. We are immediately able to see that the height of the mountain plays a critical role in both the critical velocity and vortex nucleation frequency, as expected. Even when the mountain is capped as little as to 70% of its maximal height, the number of vortices produced is visibly reduced. The vortices are generated at a sufficient frequency that secondary vortices are still formed, but in a lower quantity. For $\beta = 50\%$ even fewer vortices are produced, and for this case no clustering takes place and in turn no secondary vortices are formed. For $\beta = 40\%$ no vortices are generated at all; the reduction in height has increased the critical velocity so that $v_c > v$.

		v						
		0.15	0.25	0.35	0.45	0.55	0.65	
		100%	3	19	42	69	120	176
β	70%	0	4	21	54	85	107	
	50%	0	0	13	32	60	94	
	40%	0	0	0	18	43	53	

Table 7.1: Number of vortices, N_v , measured in the fluid at $t = 3000\tau$ over the 2D parameter space. A blue (red) shading labels the existence (lack of) a boundary layer in the resulting system.

7.3.2 Two-dimensional boundary layer

Consider Figures 7.4, 7.5 and 7.7. Notice that in all depicted cases the average height of the vortices is of the order of the highest mountain in the surface of the wire. We find for many cases throughout the parameter space that the vortices, whether as single points or as clusters, self organise in the vicinity of the surface, forming a primitive two-dimensional boundary layer with thickness on the scale of the height of the highest mountain.

In addition to the collection of vortices near the surface, for the cases where secondary clusters are formed vortex-antivortex pairs are able to pair together. In this case, they are two-dimensional analogue of vortex rings and so travel in the positive z direction, away from the boundary layer and into the bulk.

We now quantify the prevalence of the boundary layer throughout the parameter space of the system by studying the vortex distribution at late times. We define whether a boundary layer has formed in the following way. At $t = 3000\tau$ (our maximum 2D simulation time) we measure the vortex distribution. If the median vortex height is less than the height of the tallest mountain, we say the vortices have formed a boundary layer (we employ the median here as the distribution of vortex height is skewed in the positive z direction by the relatively small number of escaping vortex rings). If the median vortex height is larger than the height of the tallest mountain, we say a boundary layer has not formed. We perform simulations for a variety of truncation heights and flow velocities with the results shown in Table 7.1.

Note that the effect is not universal, for higher velocities the vortex distribution instead fills the computational box. For low (but still super-critical) velocities, the vortices are distributed in agreement with a boundary layer, but with a reduced density of vortices.

7.4 Three-dimensional results

We now move on to focus on the three-dimensional case, modelling the 3D surface by utilising the entire AFM data set. Due to the large computational requirements of a fully 3D numerical simulation of the scale required, only the full height surface (no truncation)

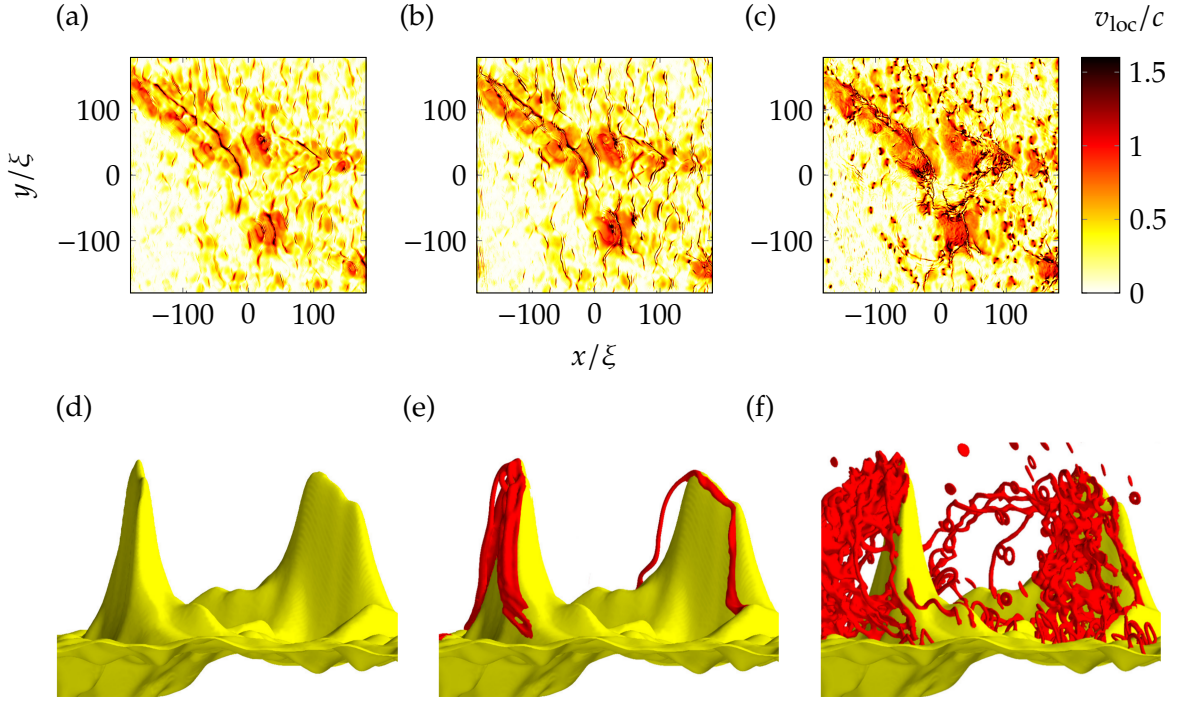


Figure 7.8: (a-c) Magnitude of the local fluid speed, $v_{\text{loc}} = |\mathbf{v}_{\text{loc}}|$, shown in the xy -plane and computed just above the surface (where the density drops to 10% of the bulk density), at three times $t = 20, 30, 100\tau$ with $v = 0.6c$. (d-f) Zoomed isosurface plots of density $n(\mathbf{r}, t)$ (plotted at 25% of the bulk density), showing the surface (yellow) and vortices (red) in the vicinity of the two tallest mountains (view taken along y over the x -range $15\xi \leq x \leq 125\xi$) at the same times.

for only a few velocities is performed.

7.4.1 Vortex nucleation from the surface

In similarity to the two-dimensional case, in the vicinity of the surface the local fluid speed, $v_{\text{loc}} = |\mathbf{v}_{\text{loc}}|$, is enhanced considerably by the surface roughness, with maximum speeds occurring near the tallest mountain. This can be seen through inspection of the local velocities near the surface, shown for several points in time in Figure 7.8 (a-c). Throughout the simulation the areas of highest velocity occur near the surface prominences seen in Figure 7.2.

As expected, up to a critical imposed velocity, the flow remains laminar and free of vortices. The critical velocity for vortex nucleation across this particular surface occurs for an imposed flow of $v_c \approx 0.2c$; this is considerably smaller than, say a hemispherical bump for which $v_c \approx 0.5c$ [240], indicating the significant role of the surface roughness in enhancing the breakdown of laminar flow, similarly to the two-dimensional case. For an increased imposed flow velocity of $v = 0.6c$, the critical velocity is first exceeded at the highest mountain, leading to nucleation of vortex lines, shown in Figure 7.8 (e), and then

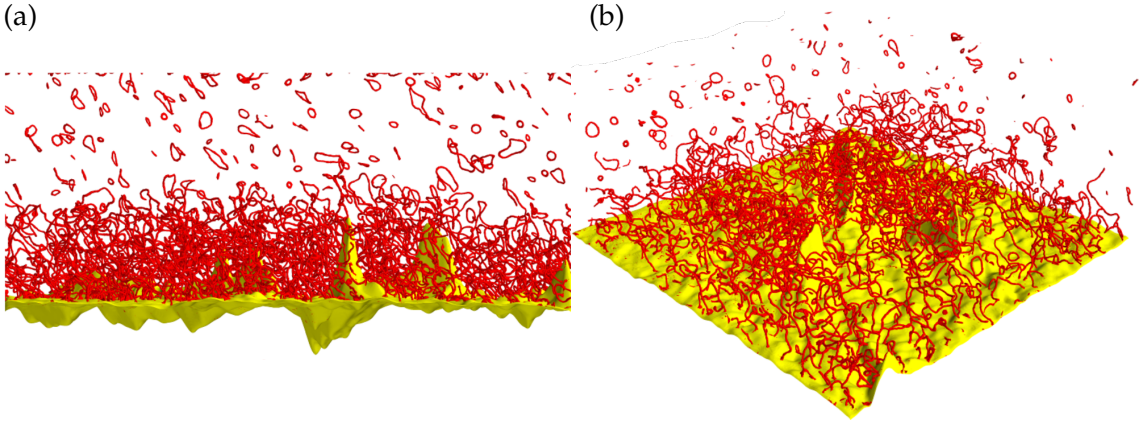


Figure 7.9: Instantaneous isosurfaces of density $n(\mathbf{r}, t)$ (plotted at 25% of the bulk density) showing the surface (yellow) and vortices (red) for a super-critical flow ($v = 0.6c$) in the saturated turbulent regime reached at long times ($t = 1220\tau$). Notice the turbulent boundary layer up to approximately the height of the highest mountains and the region of small vortex rings above it.

by other high mountains on the surface.

Nucleated vortices either peel off the boundary, or, more frequently, slide down the slopes of the mountains in the form of partially attached vortex loops (carried by the imposed flow). Nucleated vortex loops are of the same circulation and so form clusters (manifesting as partially attached vortex bundles) on the leeward side of the mountains.

The combined velocity field of the vortex bundles along with nucleation of small vortex loops throughout the surface causes an increase and spreading of areas with high local velocity near the surface, visible in Figures 7.8(b, c). The velocity field causes vortex stretching and further vortex nucleation, distorting the organised bundles of vortices and small rings into a complex tangle downstream of the mountains. The resulting tangle is continuously fed by further vortices nucleated from the surface. Vortex bundles and the beginnings of such a tangle can be seen in Figure 7.8(f). The fully developed vortex tangle in the vicinity of the surface is demonstrated in Figure 7.9.

7.4.2 Three-dimensional boundary layer

We focus on our 3D simulation with an imposed flow speed of $v = 0.6c$. For this combination of surface and flow speed, as the number of vortices increases the complex turbulent region of vortex lines remains strongly localised to the vicinity of the surface, up to approximately the height of the highest mountain. The distribution of vortices can be seen to form a distinct layer, visible in the lower half of Figure 7.9 (a). In addition to the visible layer, reconnections due to the interaction of neighbouring vortex lines causes a continuous ejection of vortex rings which spread into the bulk, visible in the upper part of Figure 7.9 (a-b).

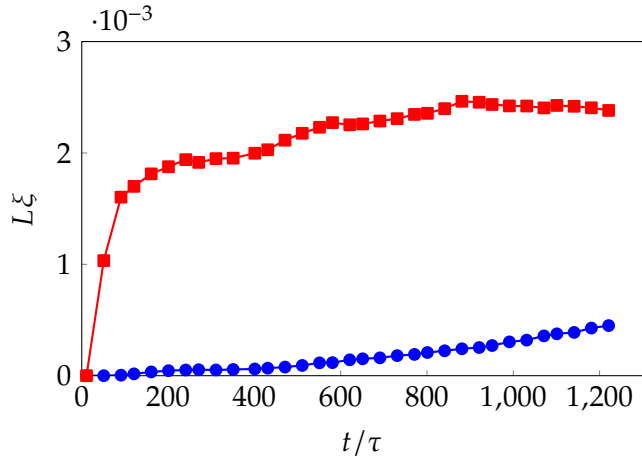


Figure 7.10: Vortex line-density below (L_0 , red squares) and above (L_1 , blue circles) the height of $z = 100\xi$, approximately the height of the tallest mountain, for a 3D simulation with imposed flow speed of $v = 0.6c$.

The turbulent layer and ejected vortex rings are not isotropic: on average, vortex lines are flattened parallel to plane of the surface and the ejected vortex rings lie more in the xy plane (so that they travel vertically away from the layer). For the slower, but still super-critical, imposed flow with speed $v = 0.2c$ the turbulent layer still forms with the same height, albeit with reduced density of vortices, generalising the behaviour of the boundary layers that formed in our 2D simulations.

Vortex line-length density

As the layer of vortices forms, the vortex line-length in the vicinity of the boundary increases with time at a much faster rate than in the bulk. However, once the layer has covered the entire computational surface, the vortex line-length within the boundary layer approximately saturates. Vortex rings continue to be ejected from the layer, and so the vortex line length in the bulk continues to slowly grow.

We quantify this behaviour by monitoring vortex line-density below and above the height of the highest mountain, L_0 and L_1 respectively. By measuring line-density in this way we are able to ascertain two things. Firstly, we will be able to measure the boundary layer's vortex line-density over time, so as we can say when the layer has saturated. Secondly, we can compare values in the region of the surface and away from the surface, as a measure of the density of the boundary layer compared to the bulk.

We split the computational box in half, with $z < 100\xi$ and $z \geq 100\xi$. We first estimate the vortex line-length in each half using the method described in Section 3.7, obtaining the vortex line-lengths for the lower and upper half of the box, $V_0(t)/A$ and $V_1(t)/A$ respectively. Finally the two quantities are used to compute the vortex line-densities L_0 and L_1

throughout the simulation, shown in Figure 7.10.

We find that both L_0 and L_1 grow over time as vortex lines are nucleated into the superfluid. L_0 quickly grows at early times, and then saturates at a value around 2.4×10^{-3} at around $t \approx 800$. On the other hand, L_1 grows much slower than L_0 and shows significantly less vortex line-density throughout the simulation, and does not saturate but instead exhibits a steady growth of vortex line-density throughout, even after L_0 has saturated at $t \approx 800$.

These measurements confirm a transient period of fast vortex line-density growth at early times which saturates in the lower half of the computational box, corresponding to the region in the vicinity of the rough surface. In addition, we observe a continuous growth of vortex line-density in the bulk, due to vortex ring formation and emission into the upper half of the computational box. This process is further investigated in Section 7.4.3.

7.4.3 Vortex ring generation through the vortex mill mechanism

At early times, nucleated vortex lines can form aligned along the flow direction, twisted due to the bundling of vortex lines nucleated at high-frequency. An example of this structure can be seen in the background of Figure 7.8 (f). The twisted vortex lines generate more vorticity which feed into the boundary layer tangle, by spooling small vortex loops through the vortex-mill mechanism envisaged by Schwarz [289]. This confirms that, for the AFM surface and an imposed flow of $v = 0.6 c$, the vortex tangle which develops can be interpreted as generated either intrinsically or extrinsically: in both cases vortices nucleate at the highest mountains before filling the layer below.

At later times (due to the modified velocity field by the saturated boundary layer) and for higher imposed flow velocities, the critical velocity is exceeded across greater areas of the surface. However, even after the generation of a considerable vortex tangle, the highest mountains continue to dominate vortex nucleation; here the fluid velocity is always the highest and vortex shedding occurs at the fastest rate. Despite this, we have already seen that the vortex line-density in the vicinity of the surface saturates at late times. To maintain equilibrium, vortex line-length is continuously ejected from the boundary layer by the process of vortex twisting, reconnections, and the formation of vortex rings that detach and travel in the positive z direction; a demonstration of this process is seen in Figure 7.11. This process provides further evidence of the presence of a vortex mill mechanism in the system, where vortex line-length is injected into the bulk of the superfluid in the form of small rings escaping the boundary layer tangle.

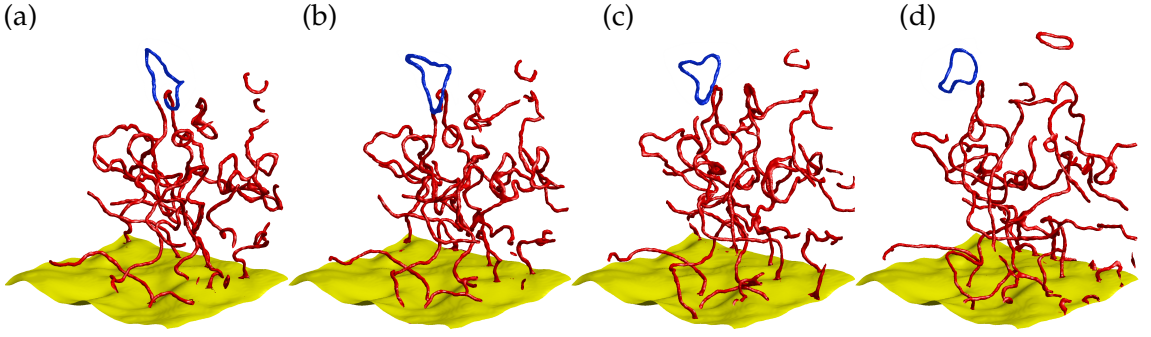


Figure 7.11: Instantaneous isosurfaces of density $n(\mathbf{r}, t)$ (plotted at 25% of the bulk density) showing the rough surface (yellow) and vortex lines (red) in the saturated regime at times $t = 730, 740, 750, 770 \tau$ and with $v = 0.6 c$. The view is of the region $120\xi < x < 196\xi, 48\xi < y < 124\xi, 20\xi < z < 160\xi$. Highlighted in blue is an escaping vortex ring (originating from the tangle) that later travels in the positive z direction and into the bulk of the fluid.

Velocity profile

We further explore the turbulent boundary layer by measuring the local velocity as a function of distance, so as to obtain a velocity profile. We measure the quantity

$$v_{xy}(z) = \langle v_{\text{loc}}(\mathbf{r}) \rangle_{xy}, \quad (7.1)$$

where $\langle v_{\text{loc}}(\mathbf{r}) \rangle_{xy}$ denotes averaging of the local fluid speed in the xy plane. We measure $v_{xy}(z)$ for all z using an average of 10 snapshots at times $1130 < t/\tau < 1220$ (so that we measure the turbulent saturated regime). The resulting quantity $v_{xy}(z)$ is a measurement of the typical local speed of the fluid flow at the height of z . For our simulation with $v = 0.6 c$, we find three regions in the profile of $v_{xy}(z)$.

In the region $100\xi \lesssim z \lesssim 200\xi$, the local flow speed is $v_{xy}(z) \approx 0.6$, showing that the fluid velocity is unaffected by the rough surface at heights of more than the height of the tallest mountain.

In the region $40 \lesssim z \lesssim 100\xi$ the presence of vortices near the surface creates a velocity field that counteracts the imposed flow velocity. The overall effect is to slow the typical flow speed the closer to the surface that it is measured, in analogy to a viscous boundary layer in classical fluids.

In the region $0 \lesssim z \lesssim 40\xi$ most of the computational volume is below the surface, and so only the fluid in the valleys is computed as part of the average. In this region the typical speed of the flow rapidly drops to almost zero.

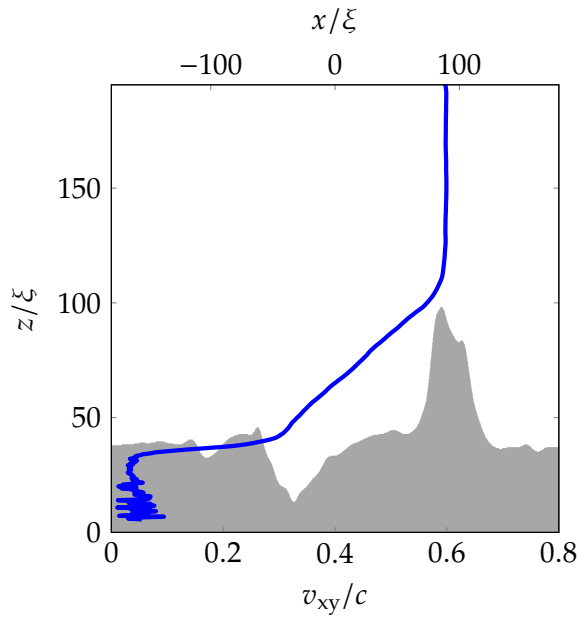


Figure 7.12: Typical local flow speed (lower abscissa) at various heights above the surface of the wire, averaged over 10 points in time, at $1130 < t/\tau < 1220$ and with $v = 0.6 c$. For comparison, a 2D sample of the 3D surface ($y = 0.1 \mu\text{m}$, demonstrating one of the tallest surface features) is shown in grey (upper abscissa).

7.5 Conclusions

In conclusion, we have modelled superflow over a real surface region of a thin NbTi ‘floppy wire’ used in helium II experiments and imaged via Atomic Force Microscopy. We have used the zero temperature GPE to numerically simulate a superfluid flow with the profile of the wire inserted using a potential term, obtaining numerical results in both 2D and in 3D.

We have performed 2D simulations and explored the parameter space of surface roughness (modified by truncation of the ‘roughest’ features in the wire) and flow velocity (imposed via a frame shift in the governing equation). For all roughness we have observed the formation of a 2D ‘boundary layer’ at certain velocities exceeding the critical velocity, consisting of a collection of quantum vortices that remain in the vicinity of the surface. We find that imposing an even higher velocity destroys the boundary layer behaviour. Our large scale 3D simulations also confirm that, for at least one set of parameters, the formation of the boundary layer generalises to three dimensions. We have shown the vortex line-density saturates over time in the layer, and have demonstrated a qualitatively similar boundary layer velocity profile as those seen in classical viscous fluids.

Our findings are a surprising result, in fluid dynamics boundary layers usually arise from viscous forces, which in superflow at absolute zero are completely absent. These

findings further illustrate the deep analogies between classical and quantum fluids.

Our results suggest that in current helium II experiments the walls of channels which confine the flow of superfluid liquid helium and the surfaces of moving objects such as wires, grids, propellers, spheres may be covered by a thin ‘superfluid boundary layer’ consisting of vortex loops and rings. The experimental implications of ‘superfluid boundary layers’ on macroscopic observables need to be investigated. This should particularly stimulate experiments in $^3\text{He-B}$, where, due to relative large healing length, it is possible to study flows with controlled surface height roughness. Our results could also be interpreted and potentially observable in the context of quasi-two-dimensional atomic BEC experiments, where recent work has enabled dynamic arbitrarily shaped obstacles, ‘painted’ with blue-detuned laser light [53].

Chapter 8

Conclusions and future work

8.1 Conclusions

In this chapter, we summarise the conclusions of the work presented throughout the thesis, and suggest relevant directions in which the work can be extended in the future.

In Part I we introduced the mean-field theory that allows for accurate modelling of a dilute, weakly interacting Bose-Einstein condensate. We described the GPE, a non-linear Schrödinger equation used to model condensates at zero temperature, along with extensions to model finite temperatures through phenomenological damping and the classical-field method. We also described the theory and practice of various numerical procedures we have used throughout the thesis.

Classical-like wakes behind elliptical obstacles in Bose-Einstein condensates

In Chapter 4 we showed that a 2D or 3D obstacle in the presence of superfluid flow in a Bose-Einstein condensate generates wakes of quantum vortices which resemble those of classical viscous flow past a cylinder or sphere.

We demonstrated a key ingredient to produce classical-like wakes: high vortex nucleation rate so that vortices undergo strong interactions with their neighbours, rather than being swept away. The role of ellipticity in this chapter was to reduce the critical velocity for vortex nucleation and increase vortex nucleation frequency and density, to facilitate strong interaction between vortices.

The symmetric wakes produced are similar to those observed in classical flow at low Re . We showed that they are unstable, forming time-dependent asymmetric structures similar to the Bénard–von Kármán vortex street of classical fluid dynamics.

The effects we described are relevant to the motion of objects such as vibrating wires, grids and forks in superfluid helium, where the obstacle’s ellipticity plays a role which is analogous to rough boundaries [243, 185], and described patterns in the density distribu-

tion that could be potentially observed in experimental atomic Bose-Einstein condensates, with moving laser-induced potentials.

Decay of 2D quantum turbulence in a highly oblate Bose-Einstein condensate

In Chapter 5 , we modelled the experimental set up of Kwon *et al.* in which the creation and decay of vortices within a BEC [101] was observed. We showed that the system is well described by simulations of the 2D-GPE with phenomenological dissipation (despite the system's technically 3D nature). We elucidated the system's experimentally unobserved early stages, showing that vortex clusters form behind a laser-induced obstacle. We demonstrated that early time symmetry breaking causes disorganisation of the vortices and that by the time the obstacle is removed, the vortices are well randomised. We confirmed the occasional appearance of crescent-shaped density features, resulting either from the proximity of vortex cores or from a sound pulse which follows a vortex-antivortex reconnection.

We showed that the vortices decay in a manner which is consistent with the two mechanisms proposed by Kwon *et al.* (loss of vortices at the condensate edge due to thermal dissipation and vortex-antivortex annihilation events within the condensate) and fitted the rate equations proposed by Kwon *et al.* and Cidrim *et al.* to the vortex decay that we observed in our numerical simulations. We concluded that Cidrim's equation fits to the data most favourably, while providing physically realistic values for the decay rates.

Quasi-classical turbulence and the critical velocity in a quenched Bose gas

In Chapter 6, we modelled a finite temperature homogeneous Bose gas. We evolved the classical field from highly non-equilibrium initial conditions, through decay of a vortex tangle, to thermalised equilibrium states with a range of temperatures and condensate fractions.

We characterised the turbulent vortex tangle by finding a kinetic energy spectrum that demonstrates a *lack* of quasi-classical turbulence, and through tracking the vortex line-density over time, we found a decay rate characteristic of ultra-quantum turbulence. We confirmed the result by calculating the velocity correlation function and integral scale, finding them to be consistent with ultra-quantum turbulence.

With the resulting equilibrium states we inserted a cylindrical obstacle with Gaussian profile, and imposed a fluid flow. We found that above the critical velocity, vortices are nucleated as wiggly vortex lines, vortex rings, or as a vortex tangle. We demonstrated that the critical velocity decreases with increasing temperature (becoming zero at the critical temperature for condensation) and scales with the square root of the condensate fraction.

Simulating the rough surface of a “Floppy Wire”

In Chapter 7, we modelled the rough surface of a real “floppy wire” used in helium II experiments through a potential term in the zero temperature GPE and by imposing a flow. The surface of the wire was provided via atomic force microscopy. We performed two-dimensional simulations of the surface at various levels of truncation and at various flow speeds to probe the parameter space.

We observed for various truncations of the 2D profile and for several flow velocities in excess of the critical velocity, the formation of a ‘boundary layer’ of quantum vortices. In each case, for a high enough imposed flow velocity the boundary layer effect breaks down and quantum vortices instead fill the computational box.

We performed large scale 3D simulations, showing the boundary layer effect generalises to three dimensions. We showed evidence of a “vortex mill” mechanism leading to escaping vortex rings formed from the boundary layer. We measured the velocity profile of the fluid flow and demonstrated a qualitatively similar profile to those seen for boundary layers in classical viscous fluids.

Our results suggest that in superfluids the surfaces of moving objects may be covered by a thin ‘superfluid boundary layer’ consisting of vortex loops and rings. This is a surprising effect: boundary layers usually arise from viscous forces, which in zero temperature superfluids are completely absent.

8.2 Future work

Other quantum analogues of classical-like wakes

Many studies of viscous flow in classical fluids have been performed over the years. Collections such as Van Dyke’s *Album of Fluid Motion* [212] demonstrate the wide range of flows possible with various obstacle shapes and sizes in both 2D and 3D regimes. As an example, the wakes of rectangular (rather than circular) obstacles and recesses are shown in Figure 8.1. Chapter 4 investigated the classical-like wakes in the simplest case of a cylinder in quantum flow. It would be an extremely interesting direction for future work to attempt to experiment with the more complicated examples of classical flow patterns that exist in the literature. The idea that the behaviour of many quantum vortices collectively reproduces classical physics would suggest that perhaps other analogies of classical fluid wakes exist in the quantum fluid realm.

Finite temperature trapped Bose gas

While the work set our in Chapter 6 is based on a homogeneous system, in reality Bose-Einstein condensates are experimentally confined in traps, rendering the gas inhomoge-

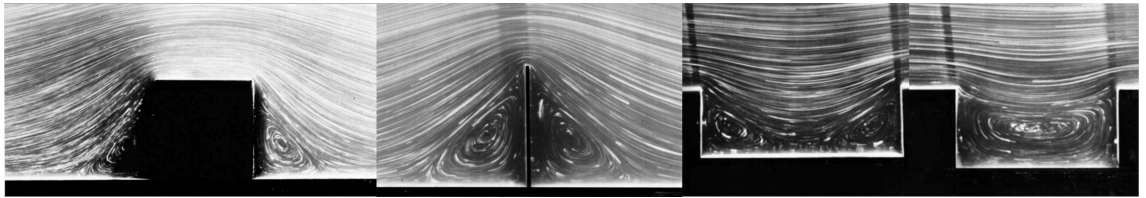


Figure 8.1: Various examples of classical viscous fluid flow around square obstacles and recesses [212].

neous. One can expect significant corrections to the critical velocity due to density gradients, as well as modifications to the vortex nucleation pattern. It would be interesting to see these higher order effects studied in future works, in particular in the common case of a harmonic trapping potential.

On the other hand, recent advances have led to the formation of quasi-homogeneous condensates in box-like traps [56, 57]. Here, the higher order corrections associated with trapping inhomogeneity should have minimal effect. An interesting direction for future experimental work would be to compare our experimentally measurable numerical predictions, such as critical velocity or the vortex line-density decay rate, to experimental data incorporating quasi-homogeneous box-like traps.

Exploring the superfluid boundary layer

The experimental implications of possible ‘superfluid boundary layers’, demonstrated in Chapter 7, on macroscopic observables needs to be investigated. The results we have shown in 3D should particularly stimulate experiments in $^3\text{He-B}$, where, due to relative large healing length, it is possible to observe vortex core structure and study flows with controlled surface height roughness.

An alternative experimental application of the 2D boundary layers observed in Chapter 7 can be found in the context of atomic BECs. Recently, the path has opened towards the realisation of dynamic and arbitrarily shaped obstacles [53]. Though this process a moving rough surface could be implemented in a quasi-two-dimensional atomic BEC.

Numerically there is also much work to still be done, particularly in 3D. While current computational limits are reached quickly with our simulations, the potential future increase in power of high performance clusters or even desktop computers could allow for quicker numerical simulation and easier visualisation of results. Along these lines, a potential extension to the work in Chapter 7 is the undertaking of a significant exploration of the 3D parameter space. It would be interesting to explore the response to changes to the imposed superfluid flow speed and surface roughness through truncation, and if the behaviour generalises from our two-dimensional results to the three-dimensional case.